J Mater Sci (2021) 56:7474–7493

Computation & theory

Particle curvature effects on microstructural evolution during solid-state sintering: phenomenological insights from phase-field simulations

Deep Choudhuri[1,*] and Logan Blake[1]

[1] *Department of Materials and Metallurgical Engineering, New Mexico Institute of Mining and Technology, Socorro, New Mexico 87801, USA*

Received: 21 December 2020
Accepted: 8 January 2021
Published online: 21 January 2021

ABSTRACT

Local curvatures have a profound influence on sintered microstructure. Here, using phase-field simulations, particle curvature effects were phenomenologically investigated by using geometrical configurations of two, three, and four particles, and by systematically varying particle curvatures. Some geometries, involving two, three and four particles, exhibited the expected smooth neck-length evolution, where the maximum neck length was determined by grain boundary (GB) energy (γ_{GB}) rather than surface energy (γ_S). In contrast, triangular arrangement of particles with unequal radii manifested a secondary necking event in form of a step during neck evolution. The secondary necking event coincided with internal pore collapse, and only specific range of particle radius ratios manifested such a mechanism. γ_S played a dominant role in triggering the secondary necking event, while γ_{GB} determined the remnant microstructure. Broadly, the geometries employed here allow us to computationally examine the sintering of particles that display wide variation in shapes and size distributions.

Introduction

Solid-state sintering is a processing technique that involves densifying green powder compacts by employing temperature, pressure or combination thereof [1–3]. This technique is used for processing high-temperature alloys, ceramics, nanocomposites [4–19] and, even, ice compacts [4, 20]. Therefore, due to the wide application of sintering, a mechanistic understanding of the processes involved is mandated, particularly from the perspective of theory and simulation that can take into account coupling of multiple competing mechanisms [1, 21, 21–27, 27–34].

The "classical" two-particle model described sintering mechanism on the basis of surface, grain boundary (GB), lattice and vapor diffusion, and GB

Handling Editor: M. Grant Norton.

Address correspondence to E-mail: deep.choudhuri@nmt.edu

https://doi.org/10.1007/s10853-021-05802-8

and surface energies [1, 21, 21–24, 35]. Such descriptions, involving kinetic and thermodynamic quantities, were used in the past to develop analytical models, or scaling laws, to quantify evolution of neck length between two particles of equal radius and their shrinkage kinetics. These scaling laws predict a smooth neck evolution, but do not allow us to view temporal change in microstructure near the neck region, i.e., they are "static" models. The description of such microstructural evolution is necessary, because technologically important powder materials increasingly contain extreme variations in size distribution, e.g., nanocomposites [14–17, 19] and shape (this category will be discussed later) [36–38].

Recent studies have shown that nano-sized powders exhibit rapid coarsening and grain boundary migration during sintering [14–17, 19, 31, 39], which is not accurately captured by the classical two-particle model [31]. Therefore, to describe such microstructural evolution, Lange *et al.* developed a thermodynamics model for two unequal sized particles, which subdivides the sintering process into three-stage processes [28, 29]. Broadly, they involve rapid neck growth (stage-I), competition between neck and grain growth (stage-II), and, finally, grain caused by rapid GB movement (stage-III). Note, Lange *et al.*'s model requires the movement of interfacial boundaries, which is not captured by the aforementioned classical model. The three-stage microstructure evolution mechanism was verified by Kumar *et al.* [31] and Ahmed *et al.* [34] by using phase-field modeling, a technique that simulates microstructure by capturing interfaces without explicitly tracking them [40, 41]. Later, Biswas *et al.* [33, 42] demonstrated that sintering kinetics can be enhanced by incorporating anisotropic microstructural properties, rigid body rotation and elastic strain energy to the phase-field models, compared to only thermodynamic considerations employed by Kumar *et al.* and Ahmed *et al.* [31, 34]. Notwithstanding, their phase-field simulations were consistent with Lange's three-stage mechanism [31, 33, 34, 42], and showed smooth neck evolution across the three stages, at least in two-particle system. Importantly, these results demonstrate that microstructural evolution during sintering is overwhelmingly driven by the thermodynamic factors, i.e., GB and surface energies [28, 29, 31, 34], rather than specific microstructural and -mechanical features.

Beyond two-particle systems, several phase-field simulations of sintering have been carried out using "diverse" ensembles, where particles are arranged in differing multi-particle geometrical configurations, e.g., triangle, linear, square, two linear rows, etc., and as polycrystalline arrangements [43–51]. Most of these studies were limited to particles of equal radii, while very few have explicitly examined the role of particle curvature on microstructural evolution [31, 52]. It is well known that particle curvature determines the local chemical potential via Gibbs–Thompson effect, and gradient of that potential drives mass transport required for neck formation and grain growth [1, 28, 29, 31, 53, 54]. Consideration of curvature effects is now even more important because of two technical applications. *First*, powder particles of vastly different shapes are increasingly used for sintering applications, e.g., particles of spherical and plate-like shapes are mixed together to form a green-compact [36–38]. *Second*, in recent years, selective laser melting is extensively used to produce porous structures [55–59]. In this additive manufacturing technique, small particles are in contact with a flat base metal plate in addition to neighbors with spherical or near-spherical curvatures (Particles may be close to a GB while in contact with the flat base plate). In other words, these two cases show that local curvatures of individual particles, and their neighbors, can vary substantially.

Thus, taking these factors into account, we have investigated the phenomenological effect of particle curvature on the evolution of sintered microstructure, e.g., neck formation, change in pore shape, GB movement and the like. For this purpose, phase-field simulations were carried out using geometrical arrangements/configurations of two, three and four particles, where local curvatures were systematically varied from zero (i.e., a flat surface) to many times the radius of the smallest grain. Our phase-field model of the sintering process is based on thermodynamic description only, i.e., incorporating only effects from GB and surface energies, because the literature suggested that such considerations can reasonably capture evolution of the sintered microstructure [31, 34]. Through this approach, we have observed unique, particle curvature-mediated microstructural mechanisms that may participate during solid-state sintering. The remainder of the manuscript is organized as follows: "Computational details and initial microstructural geometries" section

describes the phase-field model and geometrical configurations in detail, Results and analyses" section presents simulation results and corresponding analysis, and "Discussion: implications and limitations" section discusses our key findings.

Methodology

Phase-field model

Phase-field model for the sintering process was constructed using conserved ($\rho\{\vec{r},t\}$) and non-conserved ($\eta_i\{\vec{r},t\}$) variables (or order parameters). $\rho\{\vec{r},t\}$ is the solid density that acquires a value of **1** inside the solid phase and **0** with in pore regions. The non-conserved order parameter $\eta_i\{\vec{r},t\}$ (i=1,2,...,N) represents ensemble of "N" grains or particles, where η_i is **1** inside the i^{th} grain and **0** outside. Both $\rho\{\vec{r},t\}$ and $\eta_i\{\vec{r},t\}$ are related to the total free energy functional as

$$F = \int_V \left[f(\rho,\eta_i) + \frac{1}{2}\kappa_\rho |\nabla\rho|^2 + \frac{1}{2}\sum_{i=1}^{i=N} \kappa_{\eta_i} |\nabla\eta_i|^2 \right] dV, \quad (1)$$

where $f(\rho,\eta_i)$ is the bulk free energy, while the second and third gradient terms indicate excess energies due to the formation of interfaces, i.e., free surfaces and grain boundaries (GBs). In case of sintering, the gradient coefficients κ_ρ and κ_{η_i} have been shown to depend on surface and GB energies (discussed later) [31, 34, 60]. In Eq. (1), $f(\rho,\eta_i)$ was described using a Landau-type polynomial of the form [32–34, 42, 60, 61]

$$f(\rho,\eta_i) = \alpha\left[\rho^2(1-\rho)^2\right] + \beta\left[\rho^2 + 6(1-\rho)\sum_{i=1}^{i=N}\eta_i^2 - 4(2-\rho)\sum_{i=1}^{i=N}\eta_i^3 + 3\left(\sum_{i=1}^{i=N}\eta_i^2\right)^2\right], \quad (2)$$

where α and β are constants. The first term in Eq. (2) is a double-well potential, while the second term couples the conserved and non-conserved order parameters, and, taken together, both terms ensure that $f(\rho,\eta_i)$ energy landscape acquires minima within solid phase/grains and pores.

Cahn–Hilliard equation was used to describe the time evolution of the conserved order parameter ρ

$$\frac{\partial\rho}{\partial t} = \nabla\cdot D\nabla\frac{\delta F}{\delta\rho} = \nabla\cdot D\nabla\left(\frac{\partial f(\rho,\eta_i)}{\partial\rho} - \kappa_\rho\nabla^2\rho\right), \quad (3)$$

where $\frac{\partial f(\rho,\eta_i)}{\partial\rho} = \mu$ is the chemical potential, and D is the diffusion/mobility coefficient that depends on the microstructure [31, 32]. Therefore, D is assumed to be a function of $\rho\{\vec{r},t\}$ and $\eta_i\{\vec{r},t\}$ and expressed as [32]

$$D = D_{surf}\rho(1-\rho) + D_{GB}\sum_i\sum_{j\neq i}\eta_i\eta_j + D_{vol}\phi(\rho) + D_{vap}\left[1-\phi(\rho)\right]. \quad (4)$$

Eq. (4) incorporates contributions to the "net" D from surface (D_{surf}), grain boundary (D_{GB}), volumetric (D_{vol}) and vapor (D_{vap}) phase diffusion by using the interpolation function $\phi(\rho) = \rho^3(10-15\rho+6\rho^2)$. Finally, time evolution of the non-conserved order parameter η_i was computed using the Allen–Cahn equation

$$\frac{\partial\eta_i}{\partial t} = -L\frac{\delta F}{\delta\eta_i} = -L\left(\frac{\partial f(\rho,\eta_i)}{\partial\eta_i} - \kappa_\eta\nabla^2\eta_i\right), \quad (5)$$

where L is the grain boundary mobility.

Surface (γ_S) and grain boundary (γ_{GB}) interfacial energies are known well to drive mass transport during sintering, and consequently determine the evolution of microstructural features [1]. Such features include neck formation, densification and coarsening (i.e., merging small with larger grains) [31–34, 42]. Ahmed et al. have shown that γ_S and γ_{GB} are related to phase-field parameters α, β, κ_ρ and κ_η as [34]

$$\gamma_{GB} = \frac{2}{\sqrt{3}}\sqrt{\beta\kappa_\eta}, \quad \gamma_S = \frac{\sqrt{2}}{6}\sqrt{\kappa_\rho+\kappa_\eta}\sqrt{\alpha+7\beta}. \quad (6)$$

Thus, Eqs. (1)–(6) were utilized to systematically examine different types of microstructures (*c.f.* "Computational details and initial microstructural geometries" section).

Computational details and initial microstructural geometries

Numerical simulations were performed using non-dimensionalized form of Eqs. (3) and (5), as described by Ahmed *et al.* [34] and Wang [32] (In the manuscript, we will use "*" to indicate symbols corresponding to dimensionless time and length). Time integration was carried out using explicit Euler scheme with step size 0.001 (= Δt^*), and five-point stencil method for computing Laplacian (i.e., ∇^2)

[34, 60, 62–64]. These numerical techniques were utilized to conduct 2D simulations involving 128 × 128 and 256 × 256 square grids of length 0.4 (= Δx^*). Other parameters/constants present in Eqs. (1)–(6) were adapted from the literature [34, 60, 64] and are listed in Table 1. The parameters in 1st row of Table 1 (in bold) were employed in all the simulations, while 2nd and 3rd rows were used to perform sensitivity analysis for different (κ_ρ, κ_η) or (γ_S, γ_{GB}) combinations (using Eq. (6)).

Figure 1 depicts the initial microstructures/configurations used in our simulations. These configurations examine the effect of different curvature environments and grain boundaries on the evolution of sintered microstructure by using a small circular particle or grain (of radius R_{η_1}) as a "probe" (marked η_1 in Fig. 1) (In the remainder, the terms particle and grains will used interchangeably). In total, *six* cases were examined. *cases I* and *II* depict η_1 touching a larger particle with R_{η_2}=4×R_{η_1}(Fig. 1a), and a flat surface with **0** curvature or $R_{\eta_2} \to \infty$ (Fig. 1b), respectively. The two-particle configuration, similar to *case-I*, has been investigated in several phase-field based studies [31–33, 42], and, therefore, *case-I* serves as baseline/control for this work. *Case-III* examines the effect of GB, when η_1 is in contact with flat surface (Fig. 1c). *Case-IV* probes the environment around two larger circular particles η_2 and η_3, when R_{η_2} = 4×R_{η_1} and R_{η_3} = 2×R_{η_1} (*Case-IVa*, Fig. 1d1), and R_{η_2} = R_{η_3} = 4×R_{η_1} (*Case-IVb*, Fig. 1d2). Fig. 1e depicts the geometry of *Case-V*, where η_1 is simultaneously in contact with a larger particle (η_2 and R_{η_2} = 4×R_{η_1}) and a flat surface (η_3). Finally, the configuration shown in *Case-VI* (Fig. 1f) was designed to examine the effect of GB on *Case-V*. It may be pointed out that presence of an initial *internal pore* further differentiates the microstructures in cases-*IV*, *V* and *VI* from *I*, *II* and *III*. Table 2 summarizes different features of the initial geometrical configurations/microstructures.

Table 1 List of non-dimensionalized parameters used in the simulations. Mobility parameters were fixed to $D_{surf} = 10.0$, $D_{GB} = 1.6$, $D_{vol} = 0.04$, $D_{vap} = 0.002$ and $L = 1$. Computed values of γ_S and γ_{GB} for each $\{\kappa_\rho, \kappa_\eta\}$ combinations are also indicated

No.	α	β	κ_ρ	κ_η	γ_S	γ_{GB}	$\frac{\gamma_S}{\gamma_{GB}}$
1.	16	1	5	2	2.99	1.63	1.83
2.	16	1	2.5	4.5	2.99	2.45	1.22
3.	16	1	13.7	2.0	4.49	1.63	2.75

Kinetics of microstructural evolution was quantified on the basis of total neck length (l^*_{neck}), i.e., summation of neck lengths between η_1 and its immediate neighboring particles, and η_1 area (A_{η_1}) as function of time . These two temporal quantities are commonly used in the literature to quantitatively characterize microstructural evolution during sintering [1, 31–34, 42, 60, 61]. Neck length was computed using $\sum_{i\neq 1} \eta_1\eta_i(\Delta x^{*2} + \Delta x^{*2})^{\frac{1}{2}}$, and the area by $\sum_i \sum_j \eta_1 \Delta x_i^* \Delta x_j^*$ (i.e., $\int \eta_1 dA$). Simulations were carried to till the smaller η_1 particle merges with its neighbors, meaning when it disappears during the evolution process [31, 34].

Results and analyses

Simulation results are presented in the following order. In Sect . 3.1, we will discuss kinetics of small particle evolution (*c.f.* η_1 in Fig. 1) for all the *six cases* (*c.f.* Table 1). Next, on the basis of these quantitative results, we will nominally categorize the six *cases* into *fast*, *intermediate* and *slow* kinetics, and in Sects. 3.2, 3.3 and 3.4, we examine their corresponding microstructures, respectively.

Kinetics of small particle evolution

The evolution of small particle, i.e., η_1 in Fig. 1, was quantified by measuring the temporal change in three quantities for each case: (i) its total neck length or l^*_{neck} (Fig. 2a, b), (ii) area (Fig. 2c, d) and (iii) time taken by η_1 to disappear completely (Fig. 2e) . We emphasize that l^*_{neck} is summation of the length of necks formed between η_1 and its surrounding grains/particles (e.g., necks between η_2–η_1 and η_1–η_3 in *case-V* of Fig. 1d), while A_{η_1} is the area of η_1 alone.

The l^*_{neck} *v.s.* normalized time ($\frac{t^*}{t^*_{max}}$) plot in Fig. 2a compares the neck evolution in *cases I*, *II* and *III*, while Fig. 2b compares the same feature in *cases IVa-b*, *V* and *VI*. Fig. 2a shows that, in *case-I*, the neck between the smaller and larger particle (η_2) evolves in three stages (indicate as I, II and II in Fig. 2a)—consistent with literature reports [28, 29, 31, 33, 34, 42]. As exemplified using case-I in Fig. 2a, stage-I involves rapid neck formation, followed by concurrent neck and grain growth in stage-II (i.e., growth of

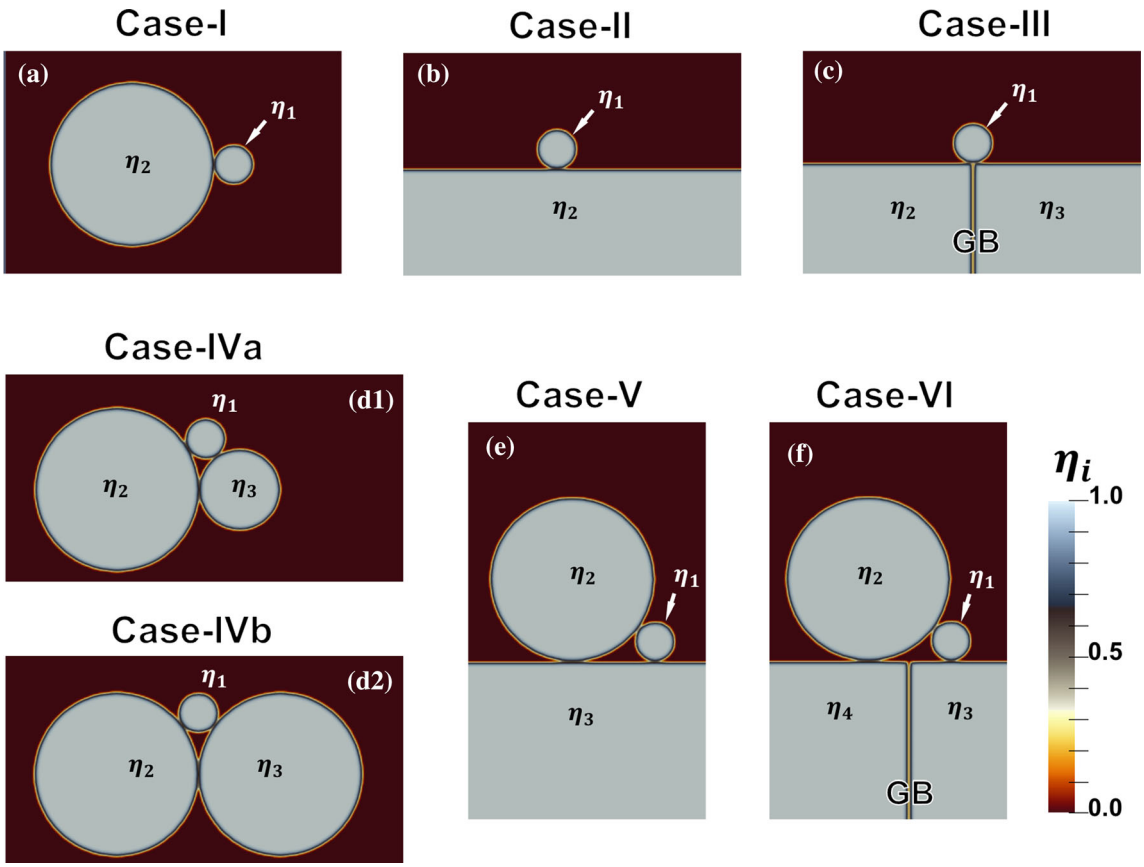

Figure 1 Initial microstructures used in the simulations. Six different cases showing the small "probe" particle (marked as η_1) in contact with larger grains/particles with differing radii/curvatures. (a) *case-I* shows the smaller in contact with a larger grain η_2 that is 4 times the radius of η_1. (b) *case-II* depicts η_1 touching a flat surface (curvature=**0**). (c) *case-III* involves a η_1 lying at the grain boundary (GB) formed by two flat-surface grains. *case-IVa* in panel (d1) shows η_1 in contact with larger circular grains, η_2 and η_3, whose radii are 4 and 2 times that of η_1, respectively. While *case-IVb* in panel (d2) contains η_1 in contact with two equal-sized circular grains with 4 times larger radius. (e) η_1 touching a larger circular grain and a flat surface (*case-V*). (f) η_1 touching a larger circular grain and a flat surface with a GB between η_1 and η_2 (*case-VI*). The radius circular grain marked η_2 in (e) and (f) is 4 times that of η_1.

Table 2 Summary of particle radii and geometry of each initial microstructures. Presence or absence of grain boundary (GB) and prior internal pore is also indicated

Case no.	η_1	η_2	η_3	η_4	Geometry	GB	Pore
I	R_{η_1}	$4\times R_{\eta_1}$	–	–	Two circular particles in contact	–	–
II	R_{η_1}	$R_{\eta_2} \rightarrow \infty^b$	–	–	Circular particle in contact with a flat surface	–	–
III	R_{η_1}	$R_{\eta_2} \rightarrow \infty^b$	$R_{\eta_3} \rightarrow \infty^b$	–	Circular particle in contact with two flat surfaces at the GB	Y	–
IVa[a]	R_{η_1}	$4\times R_{\eta_1}$	$2\times R_{\eta_1}$	–	Three circular particles forming a scalene triangle	–	Y
IVb[a]	R_{η_1}	$4\times R_{\eta_1}$	$4\times R_{\eta_1}$	–	Three circular particles forming a isosceles triangle	–	Y
V[a]	R_{η_1}	$4\times R_{\eta_1}$	$R_{\eta_3} \rightarrow \infty^b$	–	Two circular particles in contact with a flat surface	–	Y
VI[a]	R_{η_1}	$4\times R_{\eta_1}$	$R_{\eta_3} \rightarrow \infty^b$	$R_{\eta_4} \rightarrow \infty^a$	Two circular particles in contact with each other and a separate flat surface	Y	Y

[a]Contains an internal pore

[b]Represents grain/particle with a flat surface with **0** curvature

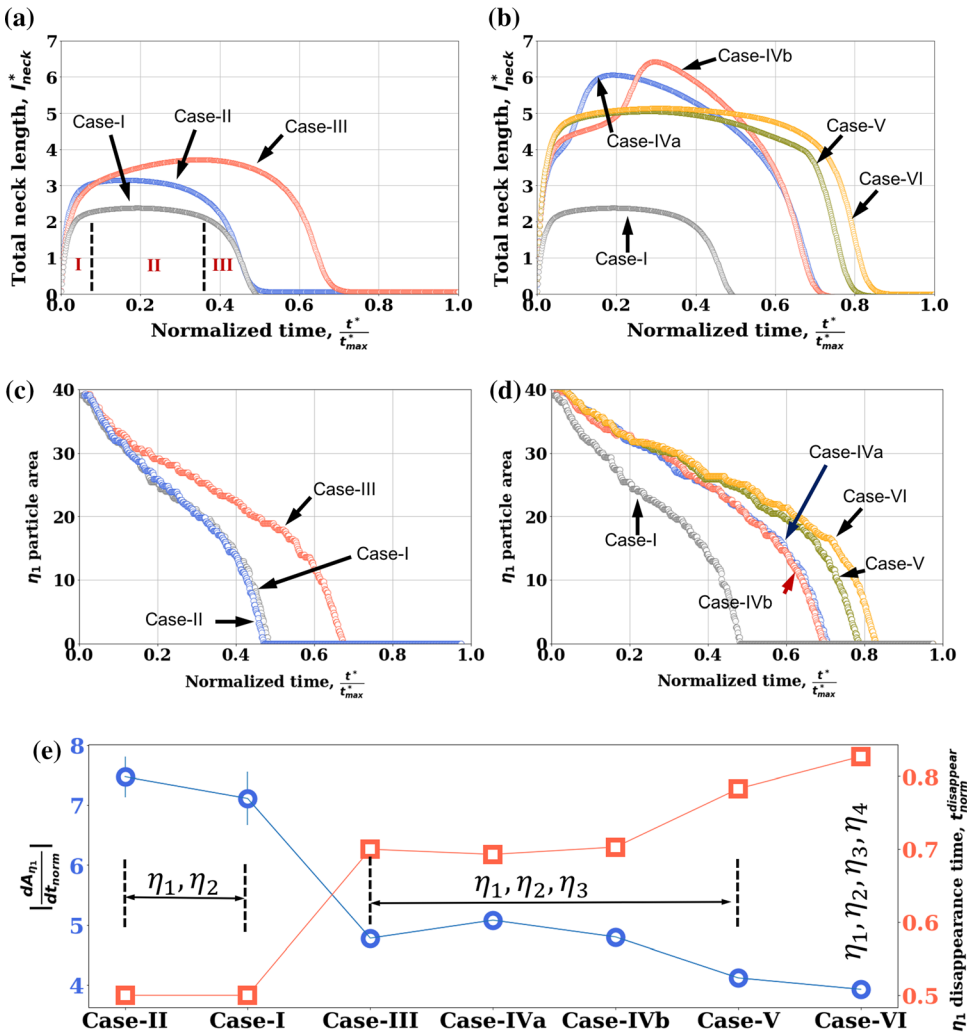

Figure 2 Plots comparing total neck-length (l^*_{neck}) evolution in (a) *cases I*, *II* and *III* and (b) *cases IVa-b*, *V* and *VI*. Except for *case-IV*, a smooth three-stage neck evolution is exhibited in all cases, i.e., initial stage of neck formation and grow, concurrent grain (the larger ones) and neck growth at the intermediate stage, and the disappearance of small grain in the final stage. As an example, the three stages are marked as I, II and II in panel (a). Panels (c) and (d) plot the change in small grain area in all *six* cases as a function of normalized time. (e) compares the magnitude of rate of areal change ($\left|\frac{\mathbf{dA}_{\eta_1}}{\mathbf{dt}_{norm}}\right|$, left axis), and time required for the small grain η_1 to disappear ($\mathbf{t}^{disappear}_{norm}$, right axis). Plots (a)–(e) were obtained using κ_ρ=5 and κ_η=2 or, γ_S=2.99 and γ_{GB}=1.63 and 128 × 128 simulation box sizes.

η_2 at the expense of η_1), and, finally, in stage-III the smaller particle is consumed by rapid GB movement [31, 34]. The last stage coincides with the disappearance of the η_1, which is seen in Fig. 2c as rapid reduction in η_1 area. Broadly, Fig. 2a, b demonstrates that *cases I*, *II*, *III*, *V* and *VI* follow the well-documented "three stage" particle evolution mechanism (also see Fig. 2c, d) (Differences between these cases will be presented later). In stark contrast, *case-IVa-b* prominently manifests an abrupt, step formation immediately after stage-I (Fig. 2b). *Case-IVa* exhibits that "step" slightly earlier than *case-IVb*, but both experience neck shrinkage and η_1 disappearance within the same time duration (shown using normalized time scale in Fig. 2b, d). In Sects. 3.3 and 3.4, we will provide a microstructural basis for the two-step mechanism. Notwithstanding, the two-step mechanism in *case-IV* distinctly highlights the effect of local curvature on the resulting microstructure. Other curvature effects can be seen in *case-II* (with a flat surface), which experiences a discernibly greater stage-II l^*_{neck} than *case-I* (see Fig. 2a). In general, l^*_{neck} at stage-II follows the trend *case-IV* > *case-V* ≈ *VI* > *case-III* > *case-II* > *case-I*.

While l^*_{neck} was computed by taking into account all possible η_1 contact surfaces, it is rather cumbersome to examine neck evolution for each contact, specially in a multi-particle environment. Therefore, we have also monitored the change in η_1 area (A_{η_1}) for each case (Fig. 2c, d), because such a quantity directly probes the influence of local curvature/radii on η_1 evolution via Gibbs–Thompson effect, i.e., $\mu \propto \frac{\gamma}{R}$ [1, 54]. In this study, by construction (see Fig. 1 and Table 1), we have varied "R", or the local curvature, for fixed values of $\gamma_{S/GB}$ (or κ_η and κ_ρ in Eq. 6). The A_{η_1} *v.s.* ($\frac{t^*}{t^*_{max}}$) plots in Fig. 2c depict the areal change in *cases I*, *II* and *III*, while, separately, Fig. 2d compares

cases IV, *V* and *VI*. A careful examination of these plots revealed two common features: *first*, an initial gradual decrease in A_{η_1} (which is later approximated using a linear fit) and, *second*, its sudden drop due to the disappearance of η_1. The latter, near-vertical drop is very likely due to rapid η_1–η_2 GB movement, which swiftly consumes the smaller η_1 grain [28, 29, 31]. Crucially, we have extracted the magnitude of rate/slope of areal reduction or $\left|\frac{\mathbf{dA}_{\eta_1}}{\mathbf{dt}_{norm}}\right|$ and the time of η_1 disappearance $\mathbf{t}_{norm}^{disappear}$ (corresponding to the moment $A_{\eta_1}=0$) from the two distinct features outlined earlier in the plots presented in Fig. 2c, d. Values of the extracted quantities are listed in Table 3, while the plot presented in Fig. 2e compares them for all cases (Fig. 1). For κ_ρ=5 and κ_η=2 (see Table 1), we find that the kinetics of η_1 evolution becomes slower by increasing the number of grains/particles, or η_i, in its neighborhood, i.e., increase in η_i decreases $\left|\frac{\mathbf{dA}_{\eta_1}}{\mathbf{dt}_{norm}}\right|$, while increasing $\mathbf{t}_{norm}^{disappear}$ (Discussion regarding the conditions that allows such a relationship between $\mathbf{t}_{norm}^{disappear}$ and number of particles will be delayed till the discussion section). A closer inspection of Fig. 2e and Table 3 revealed that η_1-kinetics can be nominally categorized into three distinct regimes, which, hereafter, will be referred to as *fast*, *intermediate* and *slow* kinetics regimes.

Fast kinetics was manifested in *cases I* and *II*, because of their highest $\left|\frac{\mathbf{dA}_{\eta_1}}{\mathbf{dt}_{norm}}\right|$ and lowest $\mathbf{t}_{norm}^{disappear}$ values among all the cases (see Fig. 2e and Table 3). *Slow* kinetics was observed in *cases V* and *VI* due to their lowest $\left|\frac{\mathbf{dA}_{\eta_1}}{\mathbf{dt}_{norm}}\right|$ and highest $\mathbf{t}_{norm}^{disappear}$ values. Accordingly, *cases III* and *IV* lay in the *intermediate* regime. It may be noted that, even though microstructures of *cases III*, *IVa-b* and *V* contained the same number of particles/grains (Fig. 1), case-V has slower η_1-kinetics than the former two microstructures (see Fig. 2e). On the other hand, the initial microstructures of *cases III* (with flat surfaces) and *IVa-b* (without flat surfaces) differed significantly in terms of local curvatures, still they manifest comparable η_1-kinetics (although neck formation mechanism is substantially different). Such contrasting kinetics within a similar category of microstructures, i.e., with same number of grains/particles, underscores the effect of local curvatures in a multi-particle environment on their microstructural evolution during sintering. In the next three subsections, we will systematically examine mechanisms contributing to the evolution of each configuration, lying within their respective each regime (Fig. 2c), in detail.

Fast kinetics regime in two-particle environments: *Cases I* and *II*

From Fig. 2e and Table 3, we find that *cases I* and *II* (with a flat surface) have comparable the rate of area reduction and disappearance time of the smaller η_1 particle. These results demonstrate that, in the two-particle configuration/geometry, flat surface has minimal impact on the η_1 evolution kinetics, at least for the chosen set of κ_ρ and κ_η (see Tables 2 and 3). However, such a surface have a noticeable influence on the neck length, where *case-II* has a longer stage-II neck than in *case-I* (Fig. 2a). To better understand this difference, we have compared and contrasted the microstructural evolution in both cases.

Microstructural evolution in *cases I* and *II* is presented in panels 3(a1)–(a3) and 3(b1)–(b3) of Fig. 3,

Table 3 List of η_1-kinetic parameters extracted from Fig. 2c, d. The slope $\left|\frac{\mathbf{dA}_{\eta_1}}{\mathbf{dt}_{norm}}\right|$ was obtained from a fit to the initial linear segment, while $\mathbf{t}_{norm}^{disappear}$ corresponds to the moment when $A_{\eta_1}=0$. Numerical simulations were performed using parameters α=16, β=1, κ_ρ=5 and κ_η=2 or, γ_S=2.99 and γ_{GB}=1.63, and 128 × 128 simulation box sizes. Additional calculations were also conducted using 256 × 256 grids to confirm the trends

η_1-kinetic params.	Case-II	Case-I	Case-III	Case-IVa	Case-IVb	Case-V	Case-VI
$\left\|\frac{\mathbf{dA}_{\eta_1}}{\mathbf{dt}_{norm}}\right\|^a$	7.47±0.34		7.11±0.44	4.78±0.12	5.08±0.07		
4.80±0.13	4.12±0.1	3.93±0.1					
$\mathbf{t}_{norm}^{disappear}$ ^{b}	0.49	0.51	0.70	0.69	0.70	0.78	0.83

[a]Dimensionless units corresponding to $\frac{[L]^2}{[T]}$

[b]Normalized time units

respectively, and shows changes from the middle of stage-II till η_1 disappears (compare Fig. 2a with Fig. 3a, b). Furthermore, the images in both cases are positioned in such a way that the movement of η_1–η_2 GB interface could be discerned. For example, in *case-I*, η_1 is observed to shrink due to GB movement (compare panels 3(a1) and 3(a2)), which is consistent with the growth of larger η_2 grain [28, 29, 31, 34]. Such GB-movement-mediated grain growth is also noted in *case-II*, although there was one key difference between the two cases. A careful comparison between panels 3(a1)–(b1) and 3(a2)–(b2) revealed that the GB in *case-II*, or the neck , had a noticeable curvature, while that neck in *case-I* is relatively flatter. Our results are also consistent with the theoretical studies by Colbeck [26], who showed that as the ratio of grain size, i.e., $\frac{R_{\eta_2}}{R_{eta_1}}$, increases the GB becomes more curved. Furthermore, our simulations reveal that the enhanced GB neck-curvature in *case-II* may have been facilitated by the formation of, diffusion-induced, protrusion on the prior flat surface (compare Fig. 3b1 and Fig. 1b). Regardless, it appears that curvature in

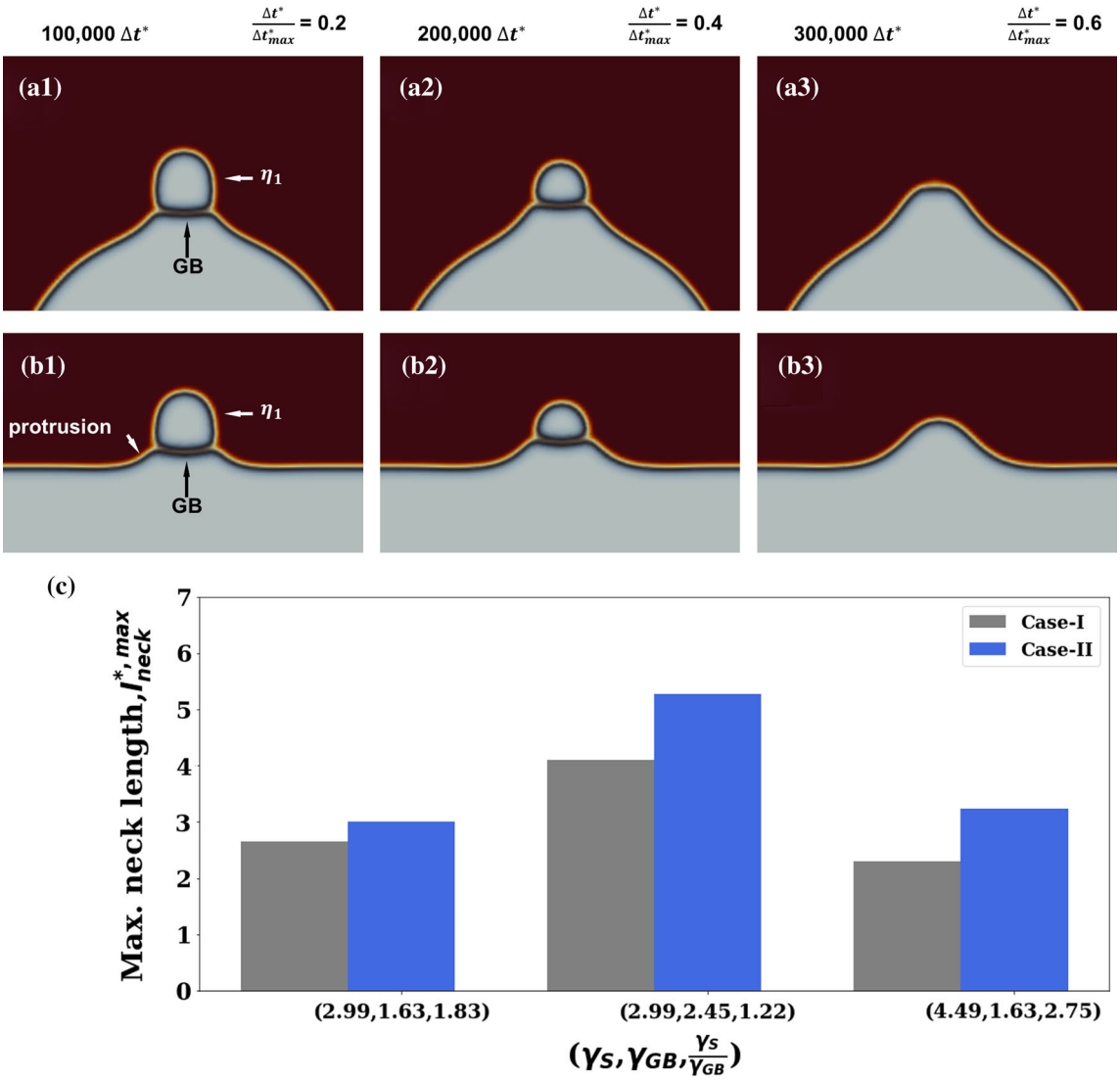

Figure 3 Time snapshots showing microstructural evolution of (a1)–(a3) *case-I* and (b1)–(b3) *case-II* at 1×10^5, 2×10^5 and $3 \times 10^5 \Delta t^*$. Corresponding normalized times, i.e., $\frac{\Delta t^*}{\Delta t^*_{max}}$, are also indicated. The microstructures in panels (a) and (b) correspond to κ_ρ=5 and κ_η=2 or, γ_S=2.99 and γ_{GB}=1.63. (c) bar chart comparing the sensitivity of maximum, stage-II, neck length ($l^{*,max}_{neck}$) to surface and grain boundary interfacial energies. *Case-II* had noticeable neck curvature and longer $l^{*,max}_{neck}$ than *case-I*. This longer $l^{*,max}_{neck}$ in *case-II* remains largely unaffected by variation in $\frac{\gamma_S}{\gamma_{GB}}$.

the neck serves to increase l^*_{neck} in *case-II*. After the disappearance of smaller particle, i.e., at the end of grain growth stage, the second grain/particle in each case (represented as η_2 in Fig. 1a, b) develops a dome-shaped protrusion on their surfaces (Fig. 3a3 and Fig. 3b3), consistent with sintered microstructures seen in many materials [4–13].

We have also systematically examined the effect of surface and GB energies on neck formation by varying the gradient coefficients κ_η and κ_ρ (see their corresponding $\gamma_S, \gamma_{GB}, \frac{\gamma_S}{\gamma_{GB}}$ in Table 1), and the *maximum total neck length* $l^{*,max.}_{neck}$ was numerically evaluated for each (γ_S, γ_{GB}) combinations (see bar chart in Fig. 3c) (Here, $l^{*,max.}_{neck}$ corresponds to the neck length during stage-II of sintering). From Fig. 3c, broadly, we find that the $l^{*,max.}_{neck}$ increases with decreasing $\frac{\gamma_S}{\gamma_{GB}}$ ratio–consistent with other two-particle sintering studies [33, 34, 42]. Note that increasing γ_{GB} (with fixed γ_S) tends to increase $l^{*,max.}_{neck}$ for both cases, while increasing γ_S (while keeping γ_{GB} fixed) reduces neck length. Importantly, Fig. 3c demonstrates that $l^{*,max.}_{neck}$ in *case-II* is consistently longer than *case-I* for all the $(\gamma_S, \gamma_{GB}, \frac{\gamma_S}{\gamma_{GB}})$ combinations, and that γ_{GB} has more influence the neck length when the smaller η_1 grain/particle is in contact with a flat surface. Therefore, our simulations show that, in a two grain/particle system, presence of a flat surface, with $R_{\eta_2} \to \infty$, enhances neck formation during the sintering process.

Intermediate kinetics regime in three-particle environments: *Cases III* and *IV*

Geometrically, by virtue of the large particle curvatures (i.e., η_2 and η_3 in Fig. 1d1–d2), *case-IV* microstructure contains an *internal triangle-shaped pore*, while, in *case-III*, contact between the flat η_2 and η_3 grains produced a GB *case-III*(Fig. 1c) (In both cases, η_1 is in contact with η_2 and η_3). Such starkly different microstructures caused little difference between their η_1-kinetics (Fig. 2e and Table 3). However, the two cases differed substantially during the stage-II of neck formation: *case-IVa-b* manifested two-step neck formation mechanism (Fig. 2b), while neck evolution in *case-III* followed a "classically" smooth stage-II transition (Fig. 2a). Therefore, to better understand the neck evolution in both cases we have carefully monitored changes in their microstructure.

Evolution of *case-III* is presented in panels (a1), (a2) and (a3) of Fig. 4, which depict microstructures near the middle of stage-II ($\frac{\Delta t^*}{\Delta t^*_{max}}$=0.4 in Fig. 2a), partial consumption of the smaller η_1 grain due to the growth of larger η_2 and η_3 grains ($\frac{\Delta t^*}{\Delta t^*_{max}}$=0.6), and the complete disappearance of η_1 at $\frac{\Delta t^*}{\Delta t^*_{max}}$ = 0.8, respectively. Here, comparable to *case-II* (Fig. 3b), neck formation involved protrusions on the flat surfaces of η_2 and η_3 (Fig. 4a1). Such protrusions grew in size, with η_1–η_2 and η_1–η_3 GBs partially consuming the smaller η_1 particle (Fig. 4a2). Fig. 4a3 shows the microstructure after stage-III (see Sect. 3.1), where η_1 has been fully absorbed by η_2 and η_3. The microstructure at $\frac{\Delta t^*}{\Delta t^*_{max}}$ = 0.8 also contained a GB groove, a feature that has been experimentally observed in many materials [65–70]. Although phase-field simulations by other groups have shown such GB grooving [52, 71–74], the current work shows that the presence of small particles at grain boundary interfaces will substantially enhance GB grooving. Focusing on neck formation, due to the presence of smaller particle at the $\eta_2 - \eta_3$-GB, the individual $\eta_1 - \eta_2$ and $\eta_1 - \eta_3$ neck lengths were half of the total neck length l^*_{neck} in Fig. 2a. (Note that the such individual neck lengths in *case-III* are smaller than in *case-II*). Sensitivity of neck formation at $\eta_2 - \eta_3$-GB was further examined by performing simulations with differing γ_{GB} and γ_S (see Table 1), and comparing the corresponding $l^{*,max.}_{neck}$ for case-III in Fig. 5a. Comparable to other cases (see Sect. 3.2), increase in γ_{GB} enhances neck formation, while γ_S does not. Combined, these results demonstrate that effect of GB on sintering of *case-III*-like configurations.

In contrast to *case-III*, the presence of an internal pore in *case-IV*, due to larger η_2 and η_3 curvatures (see Fig. 1 and Table 2), resulted in a very different neck and microstructure evolution (Fig. 4b1–b3). To illustrate this difference, for simplicity, we will focus on *case-IVb* only, while noting that both *IVa* and *IVb* configurations exhibited the two-step neck formation mechanism (Fig. 2b). In Fig. 4b1–b3, we show the microstructures resulting in the secondary (or 2^{nd}) necking event, and correlated them with the evolution of η_2–η_1–η_3 and η_2–η_3 neck formation using l^*_{neck} v.s. $\frac{\Delta t^*}{\Delta t^*_{max}}$ plots (Fig. 4c). Panel 4b1 shows the microstructure prior to the 2^{nd} neck formation event at $\frac{\Delta t^*}{\Delta t^*_{max}}$=0.15, where a triangular-shaped internal pore

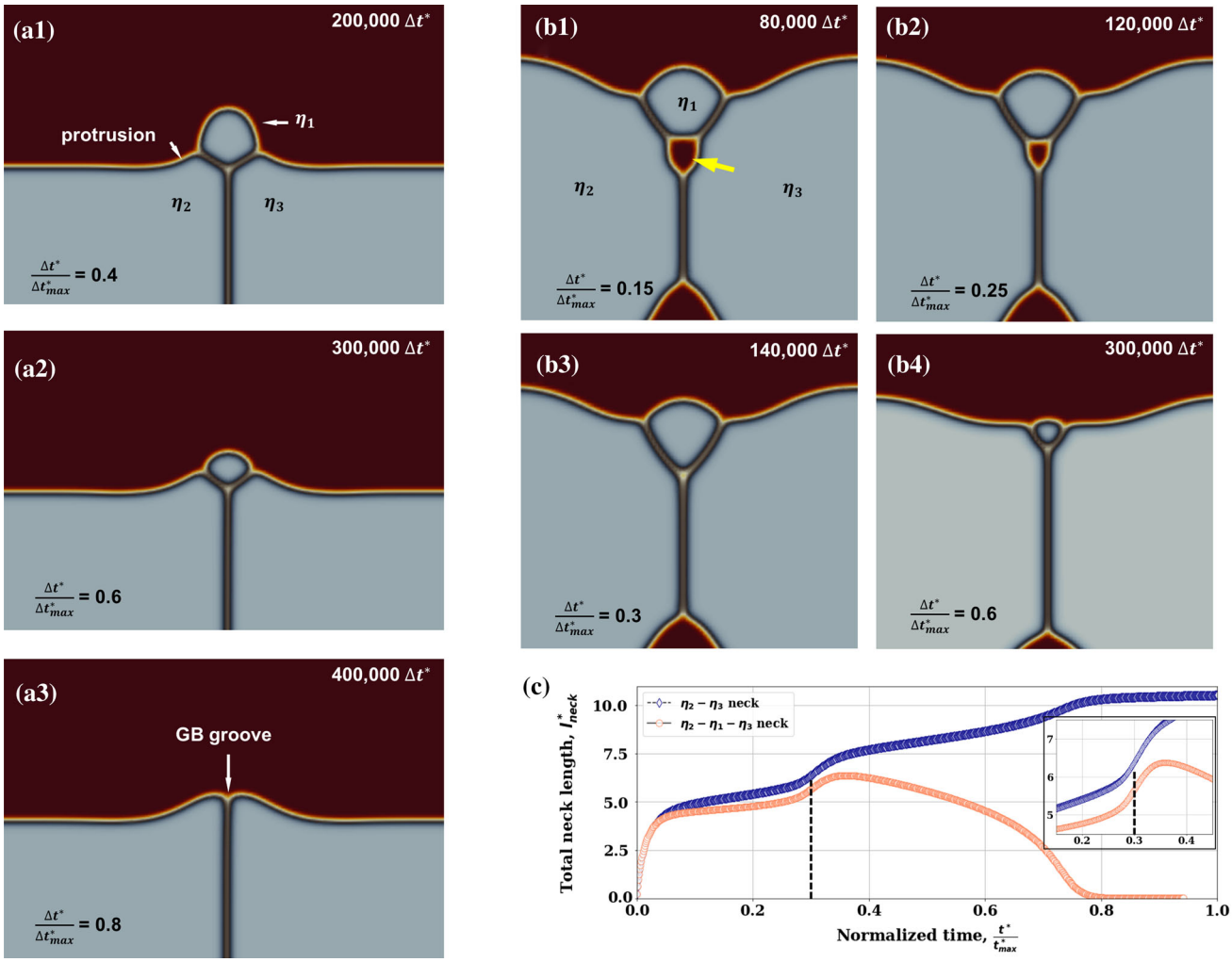

Figure 4 Snapshots showing microstructural evolution of *case-III* at (a1) 2×10^5, (a2) 3×10^5 and (a3)$4 \times 10^5 \Delta t^*$, and *case-IVb* at (b1) 0.8×10^5, (b2) 1.2×10^5, (b3) 1.4×10^5 and (b4) $4 \times 10^5 \Delta t^*$. Corresponding normalized times, i.e., $\frac{\Delta t^*}{\Delta t^*_{max}}$, are also indicated. (c) Plots comparing the development of necking between η_2–η_3 and η_2–η_1–η_3 particles with $\frac{\Delta t^*}{\Delta t^*_{max}}$. Inset in (c) shows the onset pf secondary necking event. Microstructures shown in (a) and (b) were simulated using κ_ρ=5 and κ_η=2 or, γ_S=2.99 and γ_{GB}=1.63. The smaller particle in *case-III* enhances grain boundary grooving. The collapse of the internal pore in *case-IV* causes an abrupt increase in neck length.

is trapped between the three particles (marked with an arrow). The onset of secondary event is shown in panel 4b2, at $\frac{\Delta t^*}{\Delta t^*_{max}}$=0.25 (also see the plot in Fig. 4c), where the internal pore becomes smaller. In a short span of time, at $\frac{\Delta t^*}{\Delta t^*_{max}}$=0.3, the internal pore nearly disappears or collapses (panel 4b3), which corresponded to the "rise" in secondary necking event in Fig. 4c (marked with a dotted line). Fig. 4c also shows that the secondary necking event also occurs for both η_2–η_3 between $0.25 \leq \frac{\Delta t^*}{\Delta t^*_{max}} \leq 0.3$; in addition to η_2–η_1–η_3. However, beyond $\frac{\Delta t^*}{\Delta t^*_{max}} > 0.3$, η_2–η_3 neck continues to increase, while η_2–η_1–η_3 neck length reduced monotonically after reaching its maximum value. Microstructure presented in panel 4b4 shows a snapshot within stage-III at $\frac{\Delta t^*}{\Delta t^*_{max}}$=0.6, where the η_1 particle has substantially reduced in size. We also find from Fig. 4c that η_2–η_3 neck also manifest a tertiary event at $\frac{\Delta t^*}{\Delta t^*_{max}} \sim 0.78$, when the η_1 particle disappears completely. Therefore, we learn that three-particle (circular/spherical) system, with unequal radii, will experience "abrupt" changes in the neck dimensions, due to the disappearance of smaller microstructural features during sintering. Our simulations show that such features are either small

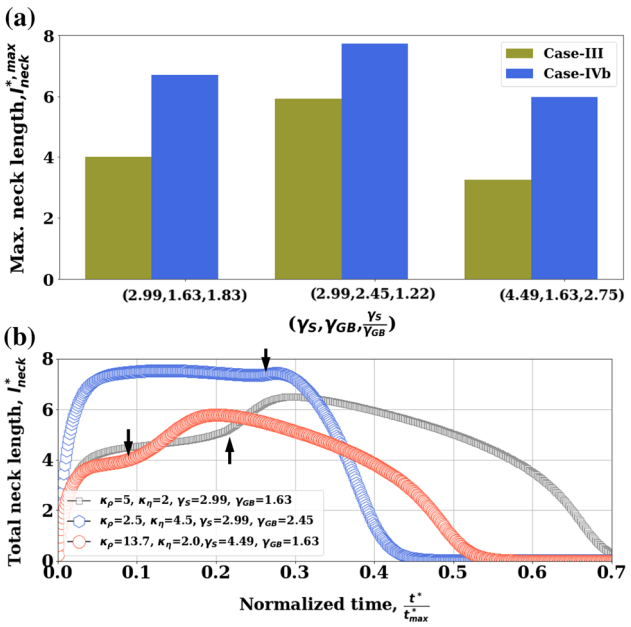

Figure 5 Plots comparing the effect of (γ_S and γ_{GB} on (a)$l^{*,max}_{neck}$ in cases *III* (olive color) and *VI* (blue color) and (b) secondary neck formation in *case-IV*. The onset of secondary event is marked with arrows in panel (b). *Case-IVb* had consistently longer neck lengths than *case-III*, irrespective of $\frac{\gamma_S}{\gamma_{GB}}$ ratio. In *case-IVb*, γ_S drives the two-step neck evolution mechanism, while the subsequent $l^{*,max}_{neck}$ was determined by γ_{GB}.

internally trapped porosity or particles themselves, and their disappearance results in a two-step formation during neck evolution (Fig. 2b and Fig. 4c).

To better understand the neck formation mechanism in *case-IV*, simulations were carried out by varying κ_ρ and κ_η (see Table 1), which allowed us to systematically vary γ_S and γ_{GB}, i.e., fix γ_S and increase/decrease γ_{GB} and vice versa, similar to other cases (Sect. 3.2). The simulation results are presented in Fig. 5a and Fig. 5b, which compares the effect of γ_S and γ_{GB} on maximum neck length $l^{*,max}_{neck}$ and secondary necking event or two-step neck formation mechanism, respectively. Fig. 5a demonstrates that $l^{*,max}_{neck}$ increases upon increasing γ_{GB} (from 1.63 to 2.45 with fixed γ_S=2.99), but decreases marginally upon reducing γ_{GB} (from 2.99 to 4.49 with fixed γ_{GB}=1.63). In other words, the maximum neck length in *case-IV* is highly dependent on γ_{GB} than γ_S—similar to cases *I*, *II* and *III*. We also find that, irrespective of γ_S and γ_{GB} values, the $l^{*,max}_{neck}$ in *case-IV* is consistently greater than *case-III* (containing flat surfaces, Fig. 4a), which suggests that, in a three-particle system, neck formation is enhanced by curved rather than flat surfaces with a GB. Interestingly, in contrast to $l^{*,max}_{neck}$, Fig. 5b shows that the two-step neck formation mechanism is strongly influenced by γ_S instead of γ_{GB}. Here, the secondary necking event is retained upon increasing γ_S (from 2.99 to 4.49 with fixed γ_{GB}=1.63), while such an event is barely visible upon increasing γ_{GB}. Thus, our simulations show that the competition between surface and GB energies are responsible for the two-step neck formation mechanism in a three-particle system. γ_S dominates till the disappearance of internal porosity (Fig. 4b1–b3), and, subsequently, γ_{GB} drives η_2–η_1–η_3 neck to acquire peak length $l^{*,max}_{neck}$ and, then, facilitates the disappearance of smaller η_1 particle via η_2–η_1 and η_3–η_1 GB movement (Fig. 4b3 and 4b4).

Slow kinetics regime in three- and four-particle environments: *Cases V* and *VI*

Cases V and *VI* exhibited largely similar neck formation (Fig. 2a) and $\mathbf{t}^{disappear}_{norm}$ (Fig. 2e) tendencies, in contrast to the cases presented Sect. 3.2 and 3.3. It may be emphasized that *case-V* is a three-particle system like *case-IV*, except that the larger η_3 grain is replaced with a flat surfaced grain, which results in a slightly elongated internal pore *case-V* than *case-IV* (see Fig. 1). Finally, in *case-VI*, we have examined the effect of grain boundary interfaces within the sintered microstructure of *case-V* by placing a GB in contact with the internal pore (Fig. 1f).

Microstructural evolution of *cases V* and *VI* is presented in Fig. 6a and 6b, respectively, which show snapshots at 1000, 100000 and 500000Δt^*. These time intervals depict microstructures at the onset of neck formation in stage-I (6a1 and 6b1), near peak neck length at stage-II (6a2 and 6b2), and the disappearance of η_1 and internal pore (6a3 and 6b3). Nominally, Fig. 6 shows that, irrespective of the GB, both cases manifest two common features: (i) similar η_1 shape evolution (unlike the other cases—see Figs. 3–5) and (ii) loss of axial symmetry in the large circular grain due to the absorption of η_1 by the surrounding grains. The latter feature is depicted by a 24° angular separation between dotted (initial axis of symmetry) and solid (axis of symmetry after η_1 disappearance) lines in Fig. 6a3 and 6b3. In case-VI, we also noted a discernible rotation/bending of the GB by 7° with respect to its initial location (see the dotted line in Fig. 6b2 and Fig. 6b3 and inset in Fig. 6b3), which

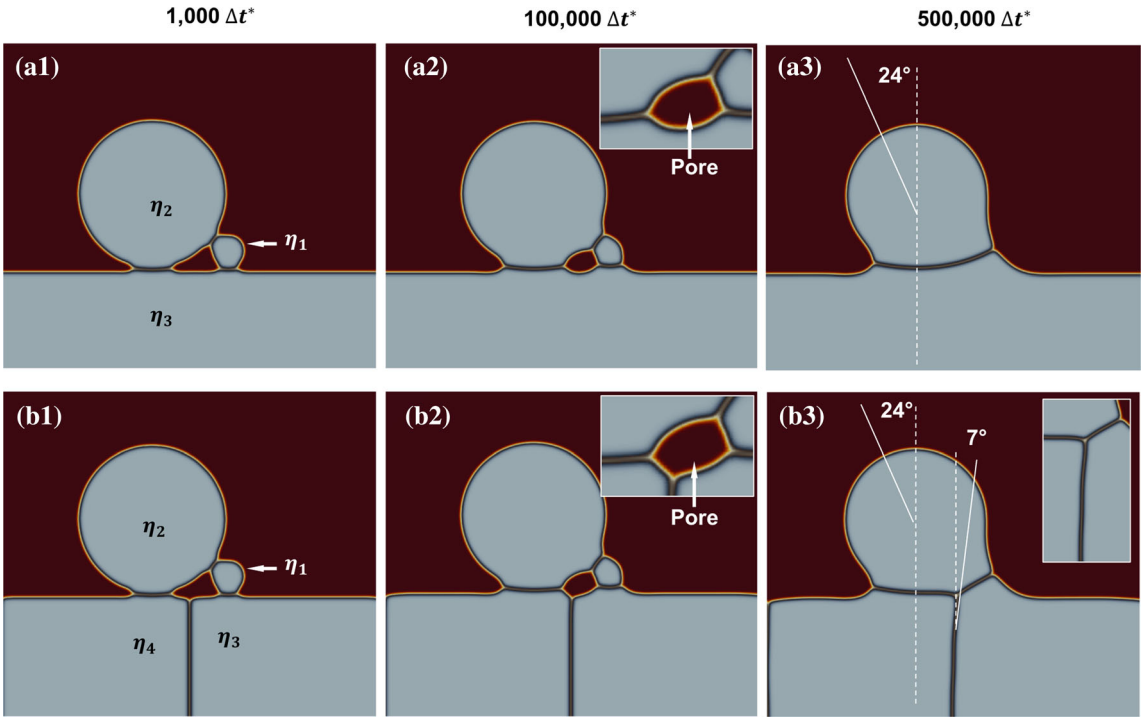

Figure 6 Snapshots showing microstructural evolution of (a1)–(a3) *case-V* and (b1)–(b3) *case-VI* at 1000, 1×10^5, and $5 \times 10^5 \Delta t^*$. (a3) and (b3) indicates loss of axial symmetry, while (b3) additionally depicts grain boundary rotation. Microstructures were obtained using κ_ρ=5 and κ_η=2 or, γ_S=2.99 and γ_{GB}=1.63. The presence of GB in *case-VI* changes the evolution pathway of the internal pore by changing its shape compared to *case-V*.

was likely caused by the disappearance of η_1 (The presence of a GB in *case-VI* also results in a triple junction in Fig. 6b3). The GBs also affected the shape of internal pores (insets in Fig. 6a2 and Fig. 6b2). In *case-V*, the triangle-shaped pore lies at a triple junction, while the additional GB in *case-VI* forces the pore to acquire a quadrilateral shape (lodged at the intersection of four GBs). Note that, in both cases, the pore is in contact with the smaller η_1 grain (marked with arrows). Next, we examine the evolution of internal pore in detail, using Fig. 7 (*case-V*) and Fig. 8(*case-VI*), which show magnified views of the region near η_1 in the same scale.

Figs. 7a, b (330000 and 340000 Δt^* for *case-V*) and 8a (330000 Δt^* for *case-VI*) qualitatively show that continued sintering have reduced the contact area between the internal pore and the smaller η_1 in both cases (compared to the microstructures at $100000\Delta t^*$ (see insets in Fig. 6a2 and 6b2)). Subsequently, *V* and *VI* develop new interfacial "neck-contacts" between the larger grains η_2 and η_3 that were in prior contact with η_1. This neck-contact is indicated using yellow colored arrows in Figs. 7c and 8b. It is worth noting that such interfacial neck-contacts separate the internal pore from η_1 in both *case-V* and *VI*, which contrasts with *case-IVb* (compared Fig. 4b1–b3 with Figs. 7c and 8b). However, the main difference between the two η_2–η_3 interfacial neck-contacts is that, in *case-V*, it lasts for very short period of time ($\approx 10000\Delta t^*$), while such a contact persists in *case-VI* for a longer duration, i.e., $\approx 10000\Delta t^*$, an order of magnitude greater than *V*. It may be pointed out that the η_2–η_3 interfacial neck-contact is essentially a grain boundary between the two grains. Subsequently, the initial η_2–η_3 interfacial neck-contact in *case-VI* evolves by elongating into an extended η_2/η_3 grain boundary (Fig. 8b-c). In the following, we will discuss how the evolution of neck-contacts changes their local environments.

The development of η_2–η_3 interfacial GB neck-contacts also alters the pore shape in both cases, in comparison their shapes at $100000\Delta t^*$(see insets in Fig. 6a2 and 6b2). In *case-V*, the pore acquires an ellipsoidal/lenticular shape, while being trapped between η_2 / η_3 bicrystal interface (Fig. 7c). On the other hand, the pore in *case-VI* had a triangle shape, and subsequent sintering time "locates" it at the η_2–η_3–η_4 triple junction (Fig. 7b). The differing shapes

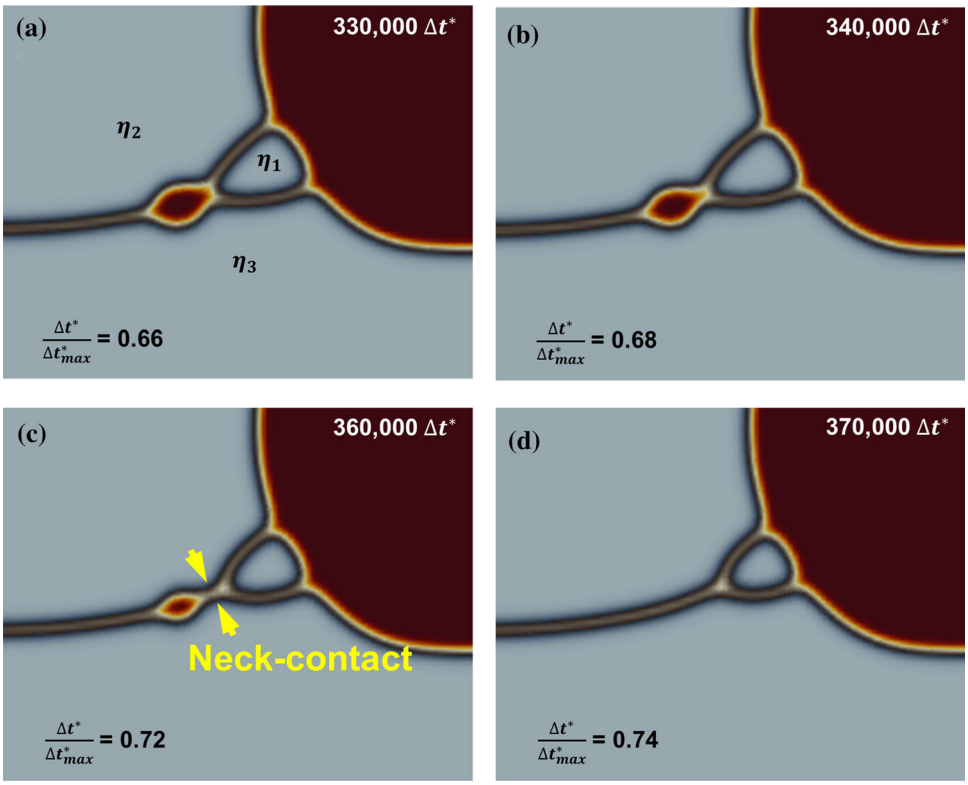

Figure 7 Snapshots showing magnified view of the microstructure near the small grain region of *case-V* at (a) 3.3×10^5, (b) 3.4×10^5, (c) 3.6×10^5 and (d) $3.7 \times 10^5 \Delta t^*$. Microstructures were obtained using κ_ρ=5 and κ_η=2 or, γ_S=2.99 and γ_{GB}=1.63. An interfacial neck-contact is noted in (c), which separates the smaller η_1 grain from the lenticular shaped pore. (d) also shows that the internal pore disappears before η_1.

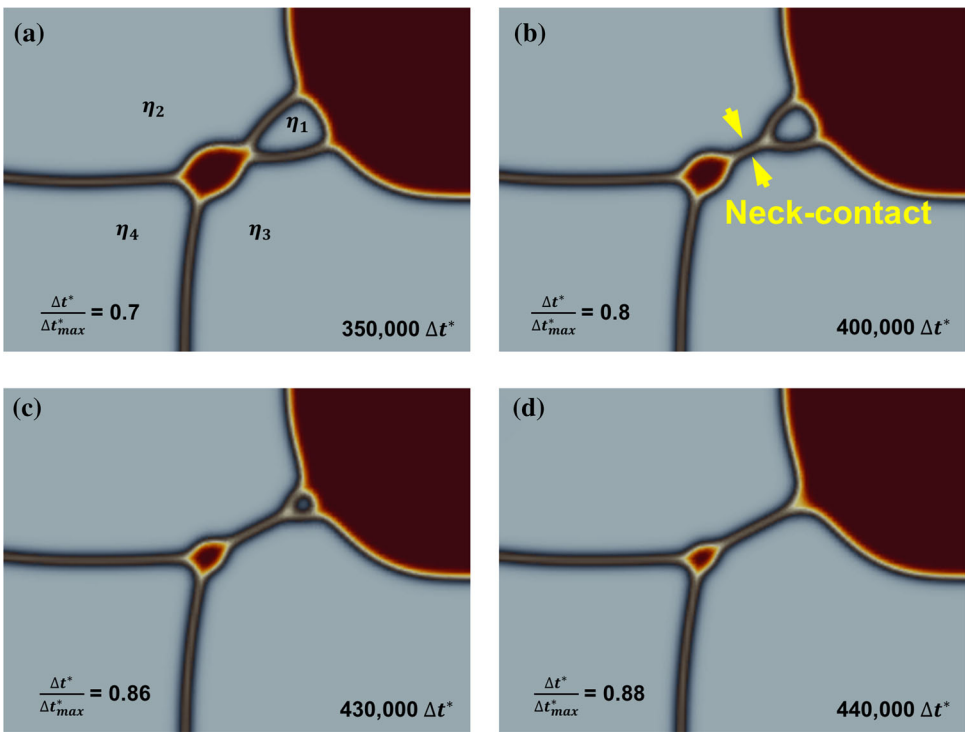

Figure 8 Snapshots showing magnified view of the microstructure near the small grain region of *case-VI* at (a) 3.5×10^5, (b) 4×10^5, (c) 4.3×10^5 and (d) $4.4 \times 10^5 \Delta t^*$. Microstructures were obtained using κ_ρ=5 and κ_η=1 or, γ_S=2.77 and γ_{GB}=1.15. An interfacial neck-contact is noted in (b), which separates the smaller η_1 grain from the lenticular shaped pore. (c) and (d) also show that η_1 disappears before the internal pore.

also determine the constrains imposed on them by the surrounding GBs, i.e., bicrystal v.s. triple junction interfaces [75–77], which, in turn influences their stability with sintering time. Evans *et al.* [75, 76], and Riedel and Svoboda [77] have shown the three GBs, at triple junction, exert a greater drag force than

bicrystal interface. Consequently, smaller drag forces on the ellipsoidal/lenticular allow it collapse sooner than the triangular-shaped pore (compare Figs. 7b and 8d), and extend the η_2–η_3 interfacial neck-contact duration in *case-VI*. The differing GB drag forces also influences the relative stabilities of the pore and smaller η_1 grain. Constrains imposed by the triple junction on the pore allows it last longer than η_1 in *case-VI* (Fig. 7), while drag forces on the bicrystal pore were insufficient to prevent it from collapsing before η_1 disappearance in case-V (Fig. 8). Therefore, the examination of *case-V* and *VI* demonstrate that the presence (or absence) of an additional GB interface in microstructures with comparable geometrical configurations produces very different grain and pore evolution pathways, e.g., compare Figs. 7d and 8d.

Pore evolution in *cases V* and *VI* can also be examined from the perspective of coordination number (N_{coord}), i.e., number of particles in contact with the pore. From Fig. 1, we note that the initial N_{coord} in *cases V* and *VI* was three and four, respectively. Kingery [21] introduced coordination number to study pore shrinkage during sintering. Later, Wakai *et al*. [78, 79] applied this notion to examine the pore shrinkage in a multi-particle environment using 3D Surface Evolver program [80], and demonstrated that pore shrinkage proceeds with progressive reduction in N_{coord}. Our 2D phase-field simulations show that, during sintering, N_{coord} in *case-V* reduces from three to two (before collapsing), and four to three in *case-VI* (Figs. 1, 6, 7 and 8). Therefore, our simulations have captured N_{coord} reduction with pore shrinkage, along with the movement of corresponding interfaces.

The *case-V* simulations further allowed us to compare and contrast with those obtained from *case-IVb*, and gather insight into their differing neck evolution tendencies (Fig. 2b): *case-IVb* exhibited two-step neck formation, while *case-V* showed a smooth stage-II transition (Both cases comprised three grains, but had different η_3 curvatures—see Fig. 1). Recall that, in *case-IVb*, the collapse of internal pore coincided with a secondary neck formation event (Fig. 4b-c), while that triangular pore remained in contact with η_1; till its final collapse prior to η_1 disappearance (Fig. 4b1–b3). In contrast, *case-V* develops an interfacial neck-contact that discernibly separates the lenticular internal pore from η_1 (Fig. 7c). Such pore-η_1 spatial interaction, i.e., contact or separation, may have influenced η_1 neck evolution. It appears that, because of the direct pore-η_1 contact in *case-IV*, the space occupied by the pore is completely consumed toward forming the η_2–η_1–η_3 interfaces, which contributes to the secondary necking event. On the other hand, in *case-V*, the space occupied by the lenticular pore is consumed to form η_2–η_3 neck, since the pore was trapped between the two grains, which have minimal impact on η_2–η_1–η_3 neck formation (A similar mechanism may be argued for case-VI). Consequently, η_1 grain in *case-V* (and *case-VI*) experienced a smoother stage-II neck evolution. Studies are in progress to gain a better mechanistic understanding of the two-step neck formation mechanism.

Furthermore, our simulations have shown that the secondary necking event is highly susceptible to γ_S (Fig. 7b). Since both cases *IV* and *V* have the same number of grains, we have conducted simulations to probe secondary neck formation in *case-V*, by varying γ_S and γ_{GB} values (Table 1) and using the approach described in Sects. 3.2 and 3.3. The results from those simulations are plotted in Fig. 9a, which did not reveal discernible secondary necking events in *case-V*. However, Fig. 9a shows that the maximum neck length depends on γ_{GB}, and is comparable to *cases I*, *II* and *III*. For sake of completion, we performed similar calculations for *case-VI* (Fig. 9b), and the results exhibited similar trends as seen in *case-V* (Comparison of Fig. 9a and 9b revealed only minor variations in the maximum neck lengths).

Discussion: implications and limitations

The systematic examination of multiple sintering geometries has revealed a unique pore-mediated, two-step neck evolution mechanism in three-particle system of unequal radii, which were organized in a triangular arrangement (Fig. 1d1–d2, Fig. 2b and Fig. 4b-c). Such a mechanism may be present in powder compacts with a wide particle size distribution [12, 13, 38, 81–83], where local arrangements may produce triangular required geometry (Fig. 1d). Furthermore, since this neck formation mechanism is determined by surface energies (see Sect. 3.3 and Fig. 5b), granular ensembles comprising particles with high surface to volume ratios may also manifest the two-step neck evolution mechanism, e.g., during the sintering of nano-sized particles [14–19]. However, the two-step neck evolution will not be

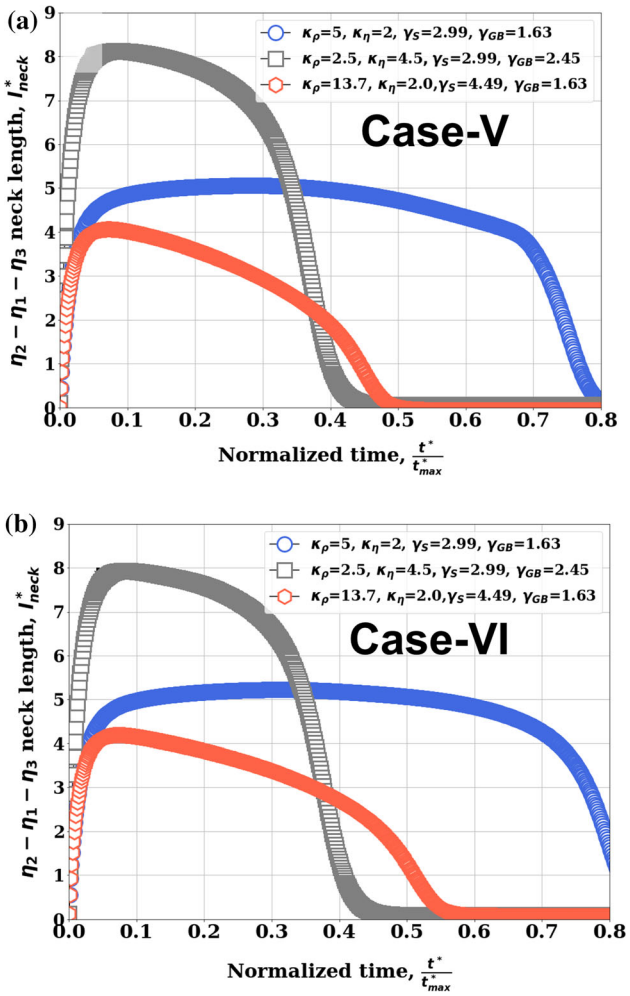

Figure 9 Plots comparing neck evolution in (a) *case-V* and (b) *case-VI* for different $(\kappa_\rho, \kappa_\eta)$ or (γ_S, γ_{GB}) combinations. Both configurations experience similar influences from varying γ_S and γ_{GB} . Only minor variations in the maximum neck lengths are barely discernible. Also not the absence of secondary necking events in panel (a), even though *case-V* have the same number of grains as *case-IV*.

exhibited for all particle sizes. To elucidate this matter, using *case-IVb*, we have examined neck evolution of geometries with different particle radius ratios (i.e., $\frac{R_{\eta_2,\eta_3}}{R_{\eta_1}}$=1,2,4,6,8) , and extracted the onset time for the secondary necking event and height of the 2^{nd} peak (exemplified using a double arrow in Fig. 10a) for each $\frac{R_{\eta_2,\eta_3}}{R_{\eta_1}}$. Fig. 10b plots the extracted quantities as a function of $\frac{R_{\eta_2,\eta_3}}{R_{\eta_1}}$. We find that the two-step neck evolution is most prominent within $2 \leq \frac{R_{\eta_2,\eta_3}}{R_{\eta_1}} \leq 6$, i.e., a regime containing clearly identifiable secondary neck onset and height (highlighted

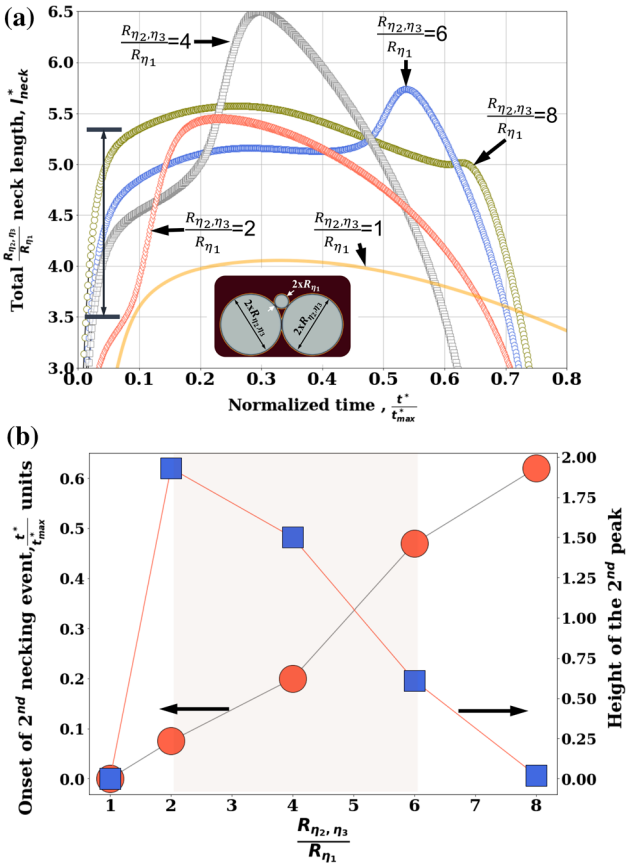

Figure 10 Plots comparing the effect of $\frac{R_{\eta_2,\eta_3}}{R_{\eta_1}}$ on the secondary neck formation in *case-IVb*. (a) shows neck evolution for $\frac{R_{\eta_2,\eta_3}}{R_{\eta_1}}$=1,2,4,6 and 8. Inset marks the radii of each grain in the three-particle system of *case-IVb*, while the double arrow in panel (a) exemplifies the secondary peak height. (b) plots the onset time for secondary necking and height the secondary peak as a function of $\frac{R_{\eta_2,\eta_3}}{R_{\eta_1}}$. Crucially, these plot demonstrate that secondary neck formation is most pronounced within a specific range, i.e., $2 \leq \frac{R_{\eta_2,\eta_3}}{R_{\eta_1}} \leq 6$ (highlighted within a box). Simulations parameters used for generating the plots were κ_ρ=5 and κ_η=2 or, γ_S=2.99 and γ_{GB}=1.63.

with a box in Fig. 10b). In contrast, this mechanism is completely absent when the particles are of equal size ($\frac{R_{\eta_2,\eta_3}}{R_{\eta_1}}$=1) and when η_2 and η_3 are substantially larger than η_1, i.e., $\frac{R_{\eta_2,\eta_3}}{R_{\eta_1}}$=8 (see inset of Fig. 10a to see the geometry). In this context, notionally, the neck evolution in *case-V* (where η_3 is a flat surface—Fig. 1e) will lie on the extreme right-hand side of Fig. 10b, since that mechanism was not seen in this configuration (Fig. 9a).

We also note that our simulations involving two-particle systems (cases *I* and *II*) did not exhibit the secondary necking events. However, Biswas *et al.* have demonstrated that two-particle system may show such events, when rigid body rotation and GB anisotropy are incorporated into Cahn–HIlliard and Allen–Cahn equations of motion (see Fig.10a in [42]). Importantly, compared to such results [42], the absence and/or presence of secondary necking events in case-*I* and *II*, and *IV*, respectively, point to a more fundamental, underlying influence of curvature and thermodynamic forces (γ_S and γ_{GB}). These influences will couple with the microstructural elements and micromechanics of sintering (as indicated in [42]), and result in a rather complex process. Such complexity behavior will arise for powders with wide size distribution and shape variations, i.e., spherical and flat surfaces, [37, 38], where the inter-particle contacts can be locally represented using a combination of case-I, II, III, IV V and V (Fig. 1).

Few comments are required regarding the effect of no. of particles/grains, and their local curvatures on the disappearance time of the smaller η_1 grain, i.e., $t_{norm}^{disappear}$. Fig. 11 examines such effects for different γ_S and γ_{GB} or, $\frac{\gamma_S}{\gamma_{GB}}$ ratios (γ_S and γ_{GB} values are listed in Table 1). Broadly, we find that $t_{norm}^{disappear}$ increases with no. of grains for $\frac{\gamma_S}{\gamma_{GB}}$=1.83 and 2.75 (marked with arrows in Fig. 11), while that effect is rather subdued for $\frac{\gamma_S}{\gamma_{GB}}$=1.22. In the latter, η_1 for *case-III* takes a longer time to disappear than the other cases, presumably because of the presence of an extended prior η_2–η_3 grain boundary (Fig 1c and Fig. 4a). Regardless, the effect of local curvature can be seen in all cases. Particularly in the configurations of three grains, i.e., cases *III*, *IVb* and *V*, where they exhibit very different $t_{norm}^{disappear}$ for a given $\frac{\gamma_S}{\gamma_{GB}}$, especially when γ_S is "significantly" greater than γ_{GB}. Furthermore, it should be noted that we have examined sintering of multi-particle systems using a phenomenological approach using $\gamma_S > \gamma_{GB}$ (Table 1); a relationship exhibited in many materials [54, 84, 85]. Therefore, the demarcation of sintering kinetics into different regimes will hold for many materials systems (Sect. 3). For example, in case of powder compacts with varying particle shape and size distributions, our results imply that sintering kinetics (leading to the final densification) will vary between locations depending on the local particle curvatures.

Finally, it may be pointed out that our phase-field simulations, while having clearly identified several particle curvature effects on neck formation, are currently constrained in two ways. *First*, these simulations were carried out using fixed values of diffusivities (see eq. 4 and Table 1). Since diffusivities are a function of temperature [53, 54], the current phase-field and geometrical models only simulate isothermal sintering. *Second*, the role of rigid body motion has been neglected [32, 33, 42]. Studies are underway to examine two-step mechanism in

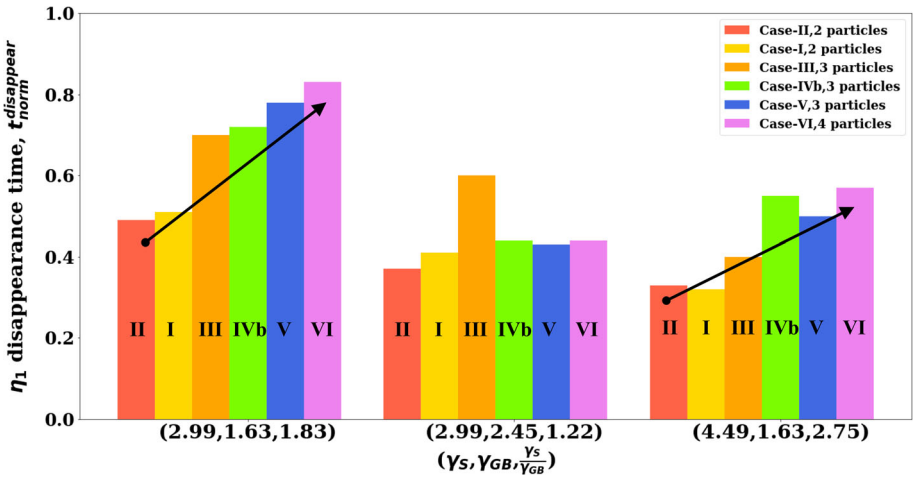

Figure 11 Bar chart comparing the effects of no. of grains, their curvature and $\frac{\gamma_S}{\gamma_{GB}}$ ratio on the η_1 grain $t_{norm}^{disappear}$. Broadly, $t_{norm}^{disappear}$ increases with the no. of grains when γ_S dominant; that trend is marked with arrows for $\frac{\gamma_S}{\gamma_{GB}}$=1.83 and 2.75. The plot also reveals noticeable differences in $t_{norm}^{disappear}$ in the configurations comprising three grains, i.e., *case-III*, *IVb* and *V*, which points the effect of differing particle/grain curvatures.

metallic alloys by taking into account both temperature variation and rigid body rotation.

Summary

In this work, we have phenomenologically investigated the effect of particle curvatures on the neck formation, and corresponding microstructural evolution, during a sintering process. Phase-field simulations were carried out using closed-packed geometrical arrangements/configurations of two, three and four particles/grains, where their local curvatures were systematically varied from zero (i.e., a flat surface) to eight times the radius of the smallest grain. Curvature effects within such geometries were characterized by the tracking neck evolution, surface area and local microstructural evolution around a "probe" grain. The influence of grain boundaries was also examined. Key findings from our simulations are as follows:

1. Some geometries, involving two, three and four particles, manifested the "classical" three-stage neck evolution mechanism, where the neck length smoothly varied from neck initiation to the final grain growth stage. The presence of flat surfaces and grain boundaries did not alter this behavior. In these geometries, local curvature affected only the maximum neck lengths. Grain boundary energy influenced the maximum neck lengths more than surface energy.
2. In contrast, neck evolution of ensembles with three circular particles of unequal radii in a closed-packed triangular arrangement, and with an internal pore trapped between the three particles, significantly departed from the classical behavior. Such a geometry consistently manifested a secondary necking event in form of a step during the neck evolution. Surface energy played a dominant role in triggering the secondary necking event, while grain boundary energy determines the remnant microstructure after the neck acquires its maximum length. Microstructurally, such a two-step neck formation mechanism is heavily influenced by the evolution of the internal pore, whose collapse (before the disappearance of the smallest grain) coincided with the secondary necking event. The secondary necking event in such three-particle ensembles was not observed for all values of particle radii. Only a range of particle radii displayed the two-step neck formation mechanism. Secondary necking event was not observed in configurations with particles of same radius, particle sizes exceed a particular ratio, or, when, one of the particle/grain had a flat surface.
3. The effect of grain boundaries on the evolution of internal pores was also evaluated using three- and four-particle configurations, while one of them was a flat surface. Our simulations showed that such boundaries can alter the pore shape and delay their collapse before the disappearance of the smallest grain. Grain boundary rotation associated with pore collapse, and the subsequent absorption of the smallest grain by the larger particles, was also captured.
4. Broadly, phase-field modeling of geometries employed here establishes the preliminary building blocks of a computational platform to investigate the sintering of powder compact, where particles display wide variation in shapes and size distributions. Studies are underway to examine secondary necking events in metallic alloys.

Acknowledgements

DC acknowledges support from New Mexico Tech's faculty startup and computer time on the Bridges2 ocean cluster through the XSEDE allocation TG-MAT200006.

Data availability

Data can be made available upon reasonable request. C++ codes developed for numerically solving equations (1)–(5) are available at https://github.com/DeepChoudhuri/Phase-field-modeling-of-Sintering.

Compliance with ethical standards

Conflict of interest The authors declare that they have no conflict of interest.

References

[1] Kang S-JL (2004) Sintering: densification, grain growth and microstructure. Elsevier, London

[2] Cavaliere P, Sadeghi B, Shabani A (2019) Spark plasma sintering: process fundamentals. Spark plasma sintering of materials. Springer, New York, pp 3–20

[3] Lóh N, Simão L, Faller C, De Noni Jr A, Montedo O (2016) A review of two-step sintering for ceramics. Ceram Int 42(11):12556–12572

[4] Blackford JR (2007) Sintering and microstructure of ice: a review. J Phys D: Appl Phy 40(21):R355

[5] Cordier A, Kleitz M, Steil MC (2012) Welding of Yttrium-doped zirconia granules by electric current activated sintering (ecas): protrusion formation as a possible intermediate step in the consolidation mechanism. J European Ceram Soc 32(8):1473–1479

[6] Diao K, Xiao Z, Zhao Y (2015) Specific surface areas of porous cu manufactured by lost carbonate sintering: measurements by quantitative stereology and cyclic voltammetry. Mat Chem Phys 162:571–579

[7] Olakanmi E, Cochrane R, Dalgarno K (2011) Densification mechanism and microstructural evolution in selective laser sintering of Al-12Si powders. J Mat Process Technol 211(1):113–121

[8] Albiter A, Leon C, Drew R, Bedolla E (2000) Microstructure and heat-treatment response of Al-2024/TiC composites. Mat Sci Eng: A 289(1–2):109–115

[9] Reimanis I, Kleebe H-J (2009) A review on the sintering and microstructure development of transparent spinel (mgal2o4). J American Ceram Soc 92(7):1472–1480

[10] Bajpai I, Han Y-H, Yun J, Francis J, Kim S, Raj R (2016) Preliminary investigation of hydroxyapatite microstructures prepared by flash sintering. Adv Appl Ceram 115(5):276–281

[11] Gregorová E, Pabst W, Uhlířová T, Nečina V, Veselỳ M, Sedlářová I (2016) Processing, microstructure and elastic properties of mullite-based ceramic foams prepared by direct foaming with wheat flour. J European Ceram Soc 36(1):109–120

[12] Sun Y, Luo G, Zhang J, Wu C, Li J, Shen Q, Zhang L (2018) Phase transition, microstructure and mechanical properties of TC4 titanium alloy prepared by plasma activated sintering. J Alloys Compd 741:918–926

[13] Reis RM, Barbosa AJ, Ghussn L, Ferreira EB, Prado MO, Zanotto ED (2019) Sintering and rounding kinetics of irregular glass particles. J American Ceram Soc 102(2):845–854

[14] Razavi-Tousi S, Yazdani-Rad R, Manafi S (2011) Effect of volume fraction and particle size of alumina reinforcement on compaction and densification behavior of al-al2o3 nanocomposites. Mat Sci Eng A 528(3):1105–1110

[15] Razavi-Tousi S, Yazdani-Rad R, Manafi S (2011) Production of Al nanocomposite reinforced by Fe-Al intermetallic, Al_4C_3 and nano-Al_2O_3 particles using wet milling in toluene. J alloys compd 509(22):6489–6496

[16] Zhang Y, Nie J, Chan JM, Luo J (2017) Probing the densification mechanisms during flash sintering of ZnO. Acta Mater 125:465–475

[17] Zhang X, Zhang Z, Wang W, Che H, Zhang X, Bai Y, Zhang L, Fu Z (2017) Densification behaviour and mechanical properties of B_4C-SiC intergranular/intragranular nanocomposites fabricated through spark plasma sintering assisted by mechanochemistry. Ceram Int 43(2):1904–1910

[18] Banerjee A, Bandyopadhyay A, Bose S (2007) Hydroxyapatite nanopowders: synthesis, densification and cell-materials interaction. Mat Sci Eng C 27(4):729–735

[19] Chaim R, Levin M, Shlayer A, Estournès C (2008) Sintering and densification of nanocrystalline ceramic oxide powders: a review. Adv Appl Ceram 107(3):159–169

[20] Szabo D, Schneebeli M (2007) Subsecond sintering of ice. Appl Phys Lett 90(15):151916

[21] Kingery W (1960) Regelation, surface diffusion, and ice sintering. J Appl Phys 31(5):833–838

[22] Coble RL (1961) Sintering crystalline solids. i. intermediate and final state diffusion models. J Appl Phys 32(5):787–792

[23] Kingery WD, Berg M (1955) Study of the initial stages of sintering solids by viscous flow, evaporation-condensation, and self-diffusion. J Appl Phys 26(10):1205–1212

[24] Coble R, Kingery W (1956) Effect of porosity on physical properties of sintered alumina. J American Ceram Soc 39(11):377–385

[25] Colbeck S (1998) Sintering in a dry snow cover. J Appl Phys 84(8):4585–4589

[26] Colbeck S (2001) Sintering of unequal grains. Journal of Applied Physics 89(8):4612–4618

[27] Kuczynski GC (1990) Self-diffusion in sintering of metallic particles, in: Sintering Key Papers, Springer, New York pp. 509–527

[28] Lange FF (1989) Powder processing science and technology for increased reliability. J American Ceram Soc 72(1):3–15

[29] Lange FF, Kellett BJ (1989) Thermodynamics of densification: II, grain growth in porous compacts and relation to densification. J American Ceram Soc 72(5):735–741

[30] Tikare V, Braginsky M, Olevsky EA (2003) Numerical simulation of solid-state sintering: I, sintering of three particles. J American Ceram Soc 86(1):49–53

[31] Kumar V, Fang Z, Fife P (2010) Phase field simulations of grain growth during sintering of two unequal-sized particles. Mat Sci Eng: A 528(1):254–259
[32] Wang YU (2006) Computer modeling and simulation of solid-state sintering: A phase field approach. Acta Mat 54(4):953–961
[33] Biswas S, Schwen D, Tomar V (2018) Implementation of a phase field model for simulating evolution of two powder particles representing microstructural changes during sintering. J Mat Sci 53(8):5799–5825
[34] Ahmed K, Yablinsky CA, Schulte A, Allen T, El-Azab A (2013) Phase field modeling of the effect of porosity on grain growth kinetics in polycrystalline ceramics. Model Simulation Mat Sci Eng 21(6):065005
[35] Herring C (1950) Diffusional viscosity of a polycrystalline solid. J appl phys 21(5):437–445
[36] Shilan ST, Mazlan SA, Ido Y, Hajalilou A, Jeyadevan B, Choi S-B, Yunus NA (2016) A comparison of field-dependent rheological properties between spherical and plate-like carbonyl iron particles-based magneto-rheological fluids. Smart Mat Struct 25(9):095025
[37] Mostafaei A, Kimes KA, Stevens EL, Toman J, Krimer YL, Ullakko K, Chmielus M (2017) Microstructural evolution and magnetic properties of binder jet additive manufactured Ni-Mn-Ga magnetic shape memory alloy foam. Acta Mat 131:482–490
[38] Mapley M, Pauls JP, Tansley G, Busch A, Gregory SD (2019) Selective laser sintering of bonded magnets from flake and spherical powders. Scripta Mat 172:154–158
[39] Groza JR (1999) Nanosintering. Nanostruct mat 12(5–8):987–992
[40] Chen L-Q (2002) Phase-field models for microstructure evolution. Annu rev mat res 32(1):113–140
[41] Provatas N, Elder K (2011) Phase-field methods in materials science and engineering. John Wiley & Sons
[42] Biswas S, Schwen D, Wang H, Okuniewski M, Tomar V (2018) Phase field modeling of sintering: Role of grain orientation and anisotropic properties. Comput Mat Sci 148:307–319
[43] Dzepina B, Balint D, Dini D (2019) A phase field model of pressure-assisted sintering. J European Ceram Soc 39(2–3):173–182
[44] Hötzer J, Seiz M, Kellner M, Rheinheimer W, Nestler B (2019) Phase-field simulation of solid state sintering. Acta Mat 164:184–195
[45] Shinagawa K (2014) Simulation of grain growth and sintering process by combined phase-field/discrete-element method. Acta Mat 66:360–369
[46] Yang Y, Ragnvaldsen O, Bai Y, Yi M, Xu B-X (2019) 3D non-isothermal phase-field simulation of microstructure evolution during selective laser sintering. NPJ Comput Mat 5(1):1–12
[47] Shinagawa K, Maki S, Yokota K (2014) Phase-field simulation of platelike grain growth during sintering of alumina. J European Ceram Soc 34(12):3027–3036
[48] Biswas S, Schwen D, Singh J, Tomar V (2016) A study of the evolution of microstructure and consolidation kinetics during sintering using a phase field modeling based approach. Extreme Mech Lett 7:78–89
[49] Zhang Z, Yao X, Ge P (2020) Phase-field-model-based analysis of the effects of powder particle on porosities and densities in selective laser sintering additive manufacturing. Int J Mech Sci 166:105230
[50] Chakrabarti T, Mukherjee R (2019) Effect of heterogeneous particle size on nanostructure evolution: A phase-field study. Comput Mat Sci 169:109115
[51] Wood M, Gao X, Shi R, Heo TW, Espitia JA, Duoss EB, Wood BC, Ye J, Exploring the relationship between solvent-assisted ball milling, particle size, and sintering temperature in garnet-type solid electrolytes, Journal of Power Sources 484 229252
[52] Asp K, Ågren J (2006) Phase-field simulation of sintering and related phenomena-a vacancy diffusion approach. Acta Mat 54(5):1241–1248
[53] Shemon P (1964) Diffusion in solids, McGraw- 33. De Schepper L., Knuyt G. and Stals L.. Phys. Stat Solidi 64
[54] Porter DA, Easterling KE (2009) Phase transformations in metals and alloys (revised reprint). CRC Press
[55] Kathuria Y (1999) Microstructuring by selective laser sintering of metallic powder. Surf Coatings Technol 116:643–647
[56] Williams JM, Adewunmi A, Schek RM, Flanagan CL, Krebsbach PH, Feinberg SE, Hollister SJ, Das S (2005) Bone tissue engineering using polycaprolactone scaffolds fabricated via selective laser sintering. Biomaterials 26(23):4817–4827
[57] Duan B, Wang M, Zhou WY, Cheung WL, Li ZY, Lu WW (2010) Three-dimensional nanocomposite scaffolds fabricated via selective laser sintering for bone tissue engineering. Acta biomat 6(12):4495–4505
[58] Xie F, He X, Cao S, Qu X (2013) Structural and mechanical characteristics of porous 316l stainless steel fabricated by indirect selective laser sintering. J Mat Process Technol 213(6):838–843
[59] Chen A-N, Li M, Wu J-M, Cheng L-J, Liu R-Z, Shi Y-S, Li C-H (2019) Enhancement mechanism of mechanical performance of highly porous mullite ceramics with bimodal pore structures prepared by selective laser sintering. J Alloys Compd 776:486–494

[60] Du L, Yang S, Zhu X, Jiang J, Hui Q, Du H (2018) Pore deformation and grain boundary migration during sintering in porous materials: a phase-field approach. J Mat Sci 53(13):9567–9577
[61] Zhang X, Liao Y (2018) A phase-field model for solid-state selective laser sintering of metallic materials. Powder Technol 339:677–685
[62] Grossmann C, Roos H-G, Stynes M (2007) Numerical treatment of partial differential equations, vol 154. Springer
[63] LeVeque RJ, Leveque RJ (1992) Numerical methods for conservation laws, vol 3. Springer
[64] Biner SB (2017) Programming phase-field modeling. Springer
[65] Mullins W, Shewmon P (1959) The kinetics of grain boundary grooving in copper. Acta Metall 7(3):163–170
[66] Saylor DM, Rohrer GS (1999) Measuring the influence of grain-boundary misorientation on thermal groove geometry in ceramic polycrystals. J American Ceram Soc 82(6):1529–1536
[67] Amram D, Klinger L, Gazit N, Gluska H, Rabkin E (2014) Grain boundary grooving in thin films revisited: the role of interface diffusion. Acta Mat 69:386–396
[68] Schölhammer J, Baretzky B, Gust W, Mittemeijer E, Straumal B (2001) Grain boundary grooving as an indicator of grain boundary phase transformations. Interf Sci 9(1–2):43–53
[69] Erk KA, Deschaseaux C, Trice RW (2006) Grain-boundary grooving of plasma-sprayed yttria-stabilized zirconia thermal barrier coatings. J American Ceram Soc 89(5):1673–1678
[70] Kelly MN, Rheinheimer W, Hoffmann MJ, Rohrer GS (2018) Anti-thermal grain growth in srtio3: Coupled reduction of the grain boundary energy and grain growth rate constant. Acta Mat 149:11–18
[71] Bouville M, Hu S, Chen L-Q, Chi D, Srolovitz DJ (2006) Phase-field model for grain boundary grooving in multicomponent thin films. Model Simulation Mat Sci Eng 14(3):433
[72] Chen P, Tsai YL, Lan C (2008) Phase field modeling of growth competition of silicon grains. Acta Mat 56(15):4114–4122
[73] Kim H-K, Kim SG, Dong W, Steinbach I, Lee B-J (2014) Phase-field modeling for 3d grain growth based on a grain boundary energy database. Model Simulation Mat Sci Eng 22(3):034004
[74] Laxmipathy VP, Wang F, Selzer M, Nestler B (2020) Phase-field simulations of grain boundary grooving under diffusive-convective conditions. Acta Mat 116497
[75] Hsueh C, Evans A, Coble R (1982) Microstructure development during final/intermediate stage sintering-i. pore/grain boundary separation. Acta Met 30(7):1269–1279
[76] Spears M, Evans A (1982) Microstructure development during final/intermediate stage sintering-ii. grain and pore coarsening. Acta Metall 30(7):1281–1289
[77] Riedel H, Svoboda J (1993) A theoretical study of grain growth in porous solids during sintering. Acta Metall et Materialia 41(6):1929–1936
[78] Wakai F, Akatsu T, Shinoda Y (2006) Shrinkage and disappearance of a closed pore in the sintering of particle cluster. Acta Mat 54(3):793–805
[79] Wakai F (2006) Modeling and simulation of elementary processes in ideal sintering. J American Ceram Soc 89(5):1471–1484
[80] Brakke KA (1992) The surface evolver. Exp math 1(2):141–165
[81] Velmurugan C, Senthilkumar V, Biswas K, Yadav S (2018) Densification and microstructural evolution of spark plasma sintered NiTi shape memory alloy. Adv Powder Technol 29(10):2456–2462
[82] Nersisyan HH, Yoo BU, Kim YM, Son HT, Lee KY, Lee JH (2016) Gas-phase supported rapid manufacturing of Ti-6Al-4V alloy spherical particles for 3D printing. Chem Eng J 304:232–240
[83] Devaraj S, Sankaran S, Kumar R (2013) Influence of spark plasma sintering temperature on the densification, microstructure and mechanical properties of Al-4.5 wt.% Cu alloy. Acta Metall Sinica (English Letters) 26(6):761–771
[84] Murr LE (1975) Interfacial phenomena in metals and alloys. Addison Wesley Publishing Company
[85] Choudhuri D, Banerjee R, Srinivasan S (2017) Interfacial structures and energetics of the strengthening precipitate phase in creep-resistant Mg-Nd-based alloys. Scientific reports 7:40540